SAND2022-1721J

Corrosion evaluation of Ti-6Al-4V manufactured by electron beam melting in Ringer's physiological solution: an in-vitro study of the passive film

Mohammadali Shahsavari*[1], Amin Imani[1], Rebecca Filardo Schaller[1,2], Edouard Asselin[1]

1. *Department of Materials Engineering, The University of British Columbia, Vancouver, BC, V6T 1Z4, Canada.*

2. *Sandia National Laboratories, Albuquerque, NM, USA*

*Corresponding author: Mohammadali Shahsavari

Email: mo.shahsavari@ubc.ca

ORCID iDs:

Mohammadali Shahsavari: https://orcid.org/0000-0002-0908-6248

Amin Imani: https://orcid.org/0000-0003-1703-0604

Edouard Asselin: https://orcid.org/0000-0001-9492-4949

Acknowledgements: The authors gratefully acknowledge the University of British Columbia for providing research facilities and financial support to conduct this research project. Also, Dr. Guilhem Martin from GPM2 group at the Université Grenoble Alpes in France and TIMET are gratefully acknowledged for providing the EBM and WR materials of this study, respectively. Sandia National Laboratories is a multimission laboratory managed and operated by National Technology & Engineering Solutions of Sandia, LLC, a wholly owned subsidiary of Honeywell International Inc., for the U.S. Department of Energy's National Nuclear Security Administration under contract DE-NA0003525. This paper describes objective technical results and analysis. Any subjective views or opinions that might be expressed in the paper do not necessarily represent the views of the U.S. Department of Energy or the United States Government. This document is SAND####.

Abstract

Electrochemical characteristics, and semiconducting behavior of additively manufactured electron beam melted (EBM) and wrought (WR) Ti-6Al-4V (Ti-G5) are compared in Ringer's physiological solution. X-ray diffraction (XRD) and field emission scanning electron microscopy (FE-SEM) confirmed the α+β structure of the tested materials, with two different microstructure types of "bimodal" and "basket-weave" for WR and EBM, respectively. Potentiodynamic

polarization (PDP) revealed that the corrosion current density for EBM (i_{corr}=0.27±0.06 μA.cm^{-2}) is less than the WR (i_{corr}=0.70±0.05 μA.cm^{-2}). Moreover, potentiostatic polarization (PS) that was employed to form the passive layers at three different potentials of 300, 500, and 700 $mV_{Ag/AgCl}$, showed that the passive films on the EBM sample are thinner. This finding was confirmed by electrochemical impedance spectroscopy (EIS). Furthermore, through Mott-Schottky (M-S) analysis, donor densities on WR passive films were found to be ~1.5 times larger than EBM. Although PS and EIS confirmed that the passive layer on EBM is thinner, it provides higher corrosion resistance than WR. The passive layer on both samples were found to have n-type characteristics with a duplex structure.

Keywords

Additive manufacturing; Biomaterials; Electron beam melting; Passive film; Ringer's solution; Titanium alloy

1. Introduction

Titanium alloys are known for their excellent engineering properties such as high corrosion resistance, biocompatibility, high stiffness to weight ratio, and high strength [1–3]. Grade 5 titanium alloy, Ti-6Al-4V (Ti-G5), classified as one of the α/β type titanium alloys, is widely used in biomedical applications due to its lightweight, corrosion resistant and human allergic response characteristics [4]. New manufacturing methods have been considered for the production of alloys with specific properties and designs, such as biomedical implants. Additive manufacturing (AM) is a newer manufacturing technique that can produce parts and objects using three-dimensional computer-aided design models in a layer-wise manner [5–7]. Using this technique, complex 3D geometries can be produced directly from raw materials [5]. Powder bed fusion (PBF), as a

subgroup of AM, includes electron beam melting (EBM), which utilizes a high energy electron beam [8, 9].

EBM technology can be considered as an effective option to increase precision for the production of biomedical implants [10, 11]. The ability to print metals with high melting points, reduced production steps, high efficiency of material use, and minimized need for post-processing are some of the advantages of EBM manufacturing [12]. These advantages of EBM make it an acceptable option to manufacture customized biomaterials and implants based on patient-specific requirements [10, 11]. Therefore, evaluation of different properties of EBM manufactured implants is essential as the final product properties are process dependent.

One of the great concerns about Ti-G5 for biomedical applications is the release of metallic ions such as Ti, Al and V, which can adversely affect the human body. The ion release effect is associated with clinical implant failure and allergic reactions that can negatively affect the implant's long-term performance [13–16]. Long-term health disorders such as Alzheimer's disease, neuropathy and osteomalacia can be caused by the Al and V ions released from Ti-G5. Previous studies have shown that V, which is alloyed with Ti as a β phase stabilizer, can form harmful oxides for the body and alter the enzyme activity kinetics that may affect the mechanisms for cell attraction to the affected area [17–21].

Different mechanisms such as corrosion, wear, and mechanically accelerated electrochemical processes could lead to metallic ion release from orthopedic implants [13–16]. Corrosion or wear processes may lead to a rise in the metal content in local or remote tissues, such as the kidney and liver. Colour changes of the surrounding tissue are often signs of implant corrosion [22]. To increase the corrosion resistance of titanium alloys for enhanced ion release, passive film growth (anodic oxidation) can be considered as a surface modification technique. This technique can grow

a passive film on the surface to increase the corrosion resistance before the implantation process [23]. However, the passive layer on the surface is not defect-free and contains point defects that can affect its properties [24].

Many studies in the literature focus on the corrosion of EBM produced alloys [7, 12, 25–28]. Concerning the surface condition, the corrosion resistance of ground EBM manufactured alloys was reported comparable to WR counterparts as opposed to the inferior corrosion resistance of selective laser melted (SLM)-produced Ti-G5 in various electrolytes [7, 12, 25, 27–30]. Some EBM microstructural features, such as its ultrafine grain structure and larger β phase content, contribute to its better corrosion resistance than the WR counterpart [12]. In terms of physiological electrolytes, there are studies in the literature about the corrosion behavior of EBM fabricated Ti-G5 in phosphate buffered saline (PBS), simulated body fluid (SBF), and Hank's solutions [12, 26–28, 31–35]. However, the investigation of corrosion and semiconducting properties of EBM produced Ti-G5 with the emphasis on orthopedic applications in Ringer's solution, which has not been reported in the literature to date, will add complementary information to the literature on EBM alloys, and valuable information for use of AM materials in orthopedic applications. The difference between PBS, SBF, and Ringer's solution is the absence of phosphates in the latter [29]. This makes Ringer's a less complex solution for corrosion evaluation of metallic biomaterials compared to other physiological solutions (e.g., PBS and SBF), leading to different corrosion and electronic properties of the passive film [29].

Ringer's physiological solution is a compatible physiological electrolyte for orthopaedical applications [22, 36–40]. Ringer's solution is also used for arthroscopic surgery which is an orthopaedical procedure for joint disorders. For an optimal joint surgery, Ringer's solution may replace the synovial fluid with the purpose of continuous irrigation. Ringer's solution is preferred

over normal saline for irrigation [39]. Moreover, a better cell tolerability for cells from the human meniscus tissue, a part of the knee cartilage, was offered by lactated Ringer's solution in comparison with the isotonic saline solution [40].

Herein, the corrosion properties of the naturally-formed and anodic oxide passive layers on EBM and WR Ti-G5 were assessed using immersion tests, open circuit potential (OCP), potentiodynamic polarization (PDP), potentiostatic polarization (PS), and electrochemical impedance spectroscopy (EIS) in Ringer's physiological solution at 37±1 °C. Further measurements were taken by Mott-Schottky analysis (M-S) to investigate the semiconducting behavior of the passive layer. Microstructural characterization was carried out using field-emission scanning electron microscopy (FE-SEM) to elucidate the influences of microstructural features on the corrosion resistance. FE-SEM micrographs were analyzed using image analysis to comparatively estimate the content of each phase. Also, X-ray diffraction (XRD) was performed for phase analysis of the material.

2. Experimental Procedure

2.1. Materials

The disc shape EBM fabricated samples were from GPM2 group at the Université Grenoble Alpes in France, produced using an ARCAM A1 EBM machine equipped with a W-filament (tungsten filament from which electrons are extracted [41]), and with an accelerating voltage of 60 kV. The standard melting themes from ARCAM were used for printing the Ti-G5 samples. The powder deposition layer in each step was 50 μm on a stainless-steel build plate [42]. The extra low interstitial (ELI) Ti-G5 metal powder (according to ASTM F3001 specifications [43]) was used in the EBM machine, and Ar gas was utilized in the atomization process to produce metallic powders with a size range of 45-105 μm. The samples' thickness and diameter were 1 and 160 mm,

respectively, and they were printed perpendicular to the build direction. TIMET provided the WR billet, with a diameter of ~4.75". The samples were known to be alpha-beta forged products and tested in the mill annealed condition. Wire cutting was employed to cut circular pieces with a diameter of 160 mm and a thickness of 2 mm. Inductively coupled plasma optical emission spectroscopy (ICP-OES) was performed after an acid digestion technique to obtain the chemical compositions of the tested alloys, and the results are presented in Table 1.

Table 1 Chemical composition of WR and EBM Ti-G5

Element (wt.%)	Fe	Al	V	Ti	Others
WR	0.09	5.82	3.94	90.1	Less than 0.05
EBM	0.10	5.93	4.11	89.8	Less than 0.05

2.2. Microstructural evaluations

The EBM and WR samples were ground to a 1200 grit finish with silicon carbide paper and then mirror polished with 0.6 μm SiC particles. Before etching, samples were rinsed with DI water and alcohol, followed by ultrasonication in acetone for 5 min to ensure contaminants removal from the grinding stage. Modified Kroll's reagent was used to etch the samples before the characterization step [12]. A Carl Zeiss Sigma FE-SEM was used to observe the microstructures of the WR and EBM samples. Then, ImageJ software was used to estimate the volume fraction of the constituent phases [44]. The phase constituents of WR and EBM alloys were also determined using X-ray diffraction by a Rigaku MultiFlex X-ray diffractometer with a 2 kW X-ray generator and a Cu-Kα radiation source.

2.3. Electrochemical measurements

A standard three-electrode flat cell with EBM and WR Ti-G5 samples as working electrodes was used for all electrochemical measurements. The exposure area of the working electrodes was 1 cm^2. Platinum (Pt) mesh was used as the counter electrode, whereas the reference electrode was silver/silver chloride (Ag/AgCl) with saturated potassium chloride (KCl) solution (+0.199 V vs. SHE). All recorded potentials herein are reported with respect to the Ag/AgCl reference electrode potential. Electrochemical measurements were performed using a PGSTAT 100 from Autolab. Before electrochemical measurements, all samples were successively ground up to 1200 grit silicon carbide paper and then washed with DI water and alcohol and then ultrasonically cleaned for 5 minutes. Samples were then dried using a high pressure compressed cold air stream. The electrolyte for electrochemical measurements was the aerated Ringer's physiological solution with the chemical composition of 8.69 g/L NaCl, 0.30 g/L KCl and 0.48 g/L $CaCl_2$ (pH=6.7). A freshly made solution with a volume of 300 mL was used for each experiment. The temperature was maintained at 37±1 °C to simulate the body temperature using circulating water from a water bath. All electrochemical measurements were repeated at least three times to ensure the reproducibility of the results, with the most representative curves presented.

Before electrochemical tests, samples were cathodically polarized at −1 $V_{Ag/AgCl}$ for 600 seconds to remove any air-formed oxide layer. The OCP tests were performed for 1 h to obtain a stable potential. Then, PDP experiments were carried out from −0.5 vs. OCP to +1.5 $V_{Ag/AgCl}$ with a scan rate of 0.166 mV/s. Three different potentials of 0.3. 0.5, and 0.7 $V_{Ag/AgCl}$ were chosen from the anodic passive region of the PDP curves (see Fig. 4). At each of these passive film formation potentials (E_f), the passive layer was formed for 1 hour using PS. Then, EIS measurements were carried out at each of these three potentials in the frequency range of 100 kHz to 10 mHz. EIS was also performed on naturally-formed oxide layers after OCP (see supplementary information).

Logarithmic sweeps of 10 points per decade were utilized for EIS analysis, and 10 mV peak-to-peak sinusoidal voltage signals were used within this experiment. The results of the EIS measurements were analyzed using the Nova 2.1 software from Autolab. EIS results were interpreted using electrochemical equivalent circuits by fitting circuit parameters through a complex non-linear least-squares technique. After EIS analysis, M-S measurements were carried out in the voltage range of the passive film formation potential up to −1 $V_{Ag/AgCl}$ with a step potential of 40 mV at 1 kHz frequency.

3. Results and discussion

3.1. Microstructure

Figure 1 shows the typical XRD patterns of WR and EBM Ti-G5 samples. The α+β structure of both alloys is clear from the peaks of the XRD patterns. As shown in Fig. 1, most of the patterns are hexagonal close-packed (HCP) α (or α') and body centered cubic (BCC) β. As both HCP α and α' share the same crystallographic structure and lattice parameters, differentiating these two phases is difficult. XRD patterns were fitted to the reported results of [12] and confirmed using the Match3! software analysis. It is seen that the respective intensities of the (100), (002), and (101) crystallographic planes (α-Ti) are higher than the others for both WR and EBM samples, consistent with other studies on Ti-G5 [12, 45]. However, the β phase peaks are relatively low due to its minor presence and, consequently, XRD had difficulty detecting this phase [46].

The β phase proportions for both WR and EBM samples were estimated using semi-quantitative analyses of XRD results using the Match! 3 software and the Reference Intensity Ratio (RIR) method. The RIR method works by scaling all diffraction data to the diffraction of standard reference materials [47]. This method assumes that the sum of all identified phases is 100%. Also, RIR assumes that there are no unidentified crystalline or amorphous phases in the tested material.

Meaningful semi-quantitative results can only be achieved when these assumptions are valid [48-50]. Therefore, RIR is not a high accuracy quantitative technique for calculation of the phase content in the material. However, it can be used for comparative studies. In spite of its limitations, the RIR method has been used for semi-quantitative analysis of different titanium alloys, including Ti-G5 [49, 51-53]. The weight fraction of the β phase in laser welded Ti-G5 samples was measured using RIR and reported to be 4%, 6%, and 7% for various welding speeds [51]. There are studies in the literature that performed atom probe tomography (APT) and reported the volume fraction of the β phase in an EBM Ti-G5 sample to be ≈4% and ≈5%, which is more convincing and accurate compared to other methods [2, 54]. However, other studies in the literature reported different β phase fraction values of around 5%, 12%, and 28% for EBM and SLM Ti-G5 samples [12, 30, 55, 56]. The discrepancies in values might stem from the different processing parameters of the various AM techniques and uncertainties associated with the quantitative analysis methods [2].

The β phase proportions (wt.%) obtained using the RIR method were approximately 12% and 7% for EBM and WR, respectively. Because of the assumptions associated with RIR [32], this technique is not considered to be a high accuracy quantitative method; however, as noted above, it can be performed for an adequate semi-quantitative and comparative analysis [43].

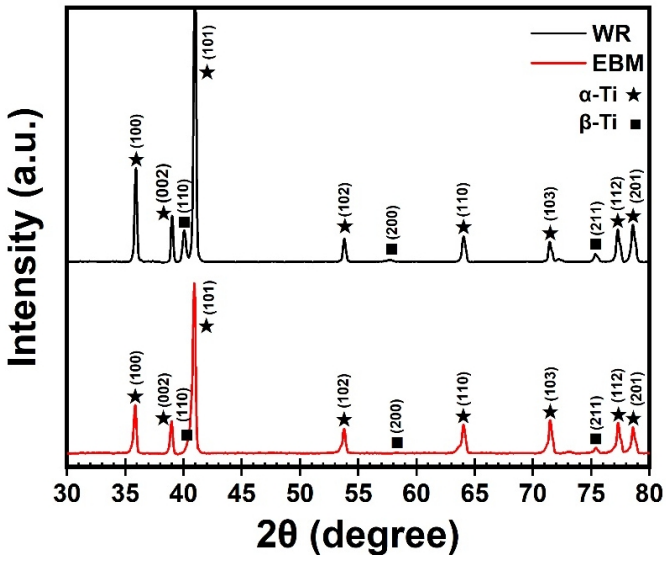

Fig. 1 XRD patterns of the EBM and WR Ti-G5 samples

Figure 2 shows the FE-SEM micrographs of the WR and EBM alloys. For the WR sample (Fig. 2 (a)), equiaxed α grains with the intergranular β phase are seen in the microstructure, which is known as "bimodal." In this type of microstructure, in addition to the equiaxed α grains, some α lathes can be detected with the same Burgers orientation relationship to the β phase. However, the Burgers orientation relationship between the equiaxed α and β phases is not the same [58]. This type of microstructure appears when the heat treatment temperature is below the β-transus temperature, but still in the α+β region. The described microstructure is for the typical annealed Ti-G5 sample which has been held for long periods under the β-transus temperature [58,59]. The strong oxidizing power of the Kroll's reagent can etch out the α phase, so it looks darker in contrast compared to the β phase. The β phase looks brighter in FE-SEM images [12].

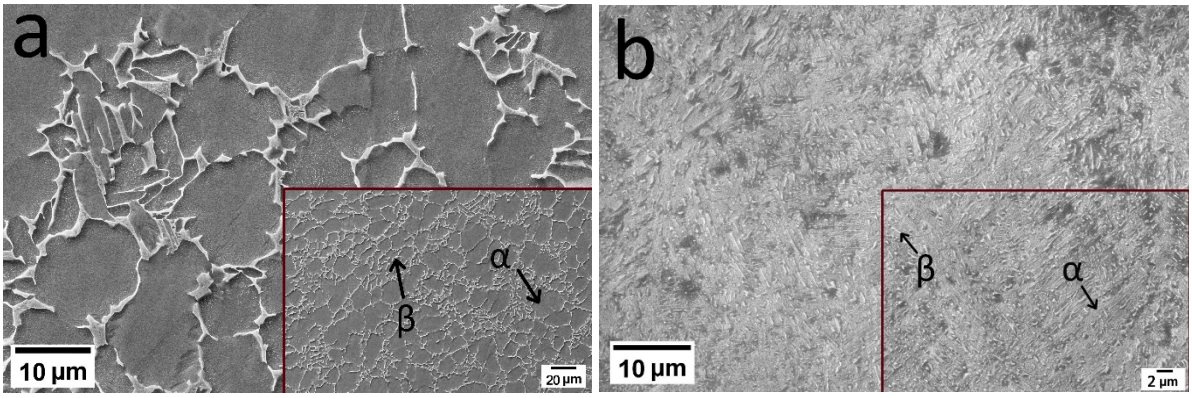

Fig. 2 FE-SEM images of (a) WR and (b) EBM Ti-G5 microstructures. The light grey areas are the beta phase while the darker grey areas are the alpha phase

The microstructure of the EBM sample is shown in Fig. 2 (b). This is a "basket-weave" microstructure, which is consistent with other studies [2, 12]. During the cooling process, the α phase precipitates from the β phase, and then lath or plate-like features appear in the morphology, separated by β ribs. In the condition where the cooling rate is fast, the laths might not arrange in a parallel structure of five or more through the nucleation and growth process. As a result, the final morphology shows a weave-like structure, in and out of the laths, which is why it is referred to as a "basket-weave" microstructure [58, 59]. Figure 2 (b) shows a sandwiching structure of β/α/β that was formed of singular α bulges and prior β grains [2, 12]. As shown in Fig. 2, both WR and EBM Ti-G5 microstructures consist of α and β phases arranged in different morphologies dependent on the different manufacturing processes. Microstructure images also showed that the grains in WR are coarser compared to EBM, where a dot-like morphology was observed.

3.2. Volume fraction of the β phase

Figure 3 demonstrates the processed FE-SEM images using ImageJ to estimate the volume fraction of the β phase. To minimize the potential inaccuracies, five different FE-SEM images for WR and EBM were considered and the average value is reported. From the results of the microstructural analysis, ≈ 20% of the morphology is occupied by the β phase in the EBM sample, whereas this value for the WR sample is ≈ 13%, which confirmed that the β phase content was more considerable in EBM than the WR counterpart. Similar amounts were reported in the literature for differently manufactured and processed Ti-G5 alloys [12, 30, 45, 55,56].

The literature contains several studies on phase quantification of titanium alloys using image analysis by different software, including ImageJ [57, 58, 60-68]. Various procedures have been reported for phase quantification using image analysis. Although some studies explain the exact procedure for the phase quantification and image analysis, there are studies in the literature that did not describe the methodology [61, 62, 66, 68]. For example, in a study on Ti-6Al-2Sn-4Zr-6Mo(Ti-6246), the "Auto Threshold" option was performed on as-collected SEM-BSe images, without performing any prior processing (e.g. brightness, contrast, sharpness adjustments) [57]. Due to the errors associated with the manual "Threshold", the "Auto Threshold" was chosen instead [57]. Cao et al. also used "Threshold" for variously heat treated SLM Ti-G5 samples to estimate the volume fraction of the β phase [63]. In another work on Ti-G5 samples produced by direct energy deposition (DED), optical microscopy micrographs of WR and DED samples converted to binary images and used for the analysis. When using the binary images, the α phase displays in white pixels and the β phase displays in black pixels, or vice versa [64].

Although the discussed procedures for image analysis can estimate the phase fractions to some extent, different factors affect the accuracy of the results. For example, variations in resolution, preparation methods, brightness, and contrast can create errors in final results [57]. Also, the

"Threshold" option in ImageJ software is sensitive to the mentioned variables and, therefore, can report inaccurate results where the picture processing and contrast adjustments are not sufficient [57].

In the present study, after noise reduction, contrast adjustment, and surface smoothing (to reduce the effect of dot-like particles [62]), the "Auto Threshold" option (using binary images) was applied on FE-SEM micrographs of WR and EBM samples. The over-etched areas in some FE-SEM micrographs and insufficient contrast between phases in some images could be potential reasons for inaccurate results. When the SEM micrographs contain over-etched areas or dark regions, the phase quantification using image analysis by ImageJ may only prove useful for comparative studies and semi-quantitative analysis. Therefore, the obtained values for β phase content in this study were considered only for comparison between WR and EBM samples.

The β phase constituents for the EBM Ti-G5 obtained from semi-quantitative analysis of XRD and FE-SEM images were 12% (wt.%) and 20% (vol.%), respectively. These values for the WR sample were 7% (wt.%) and 13% (vol.%). Therefore, by comparison, the EBM sample seems to have a larger β phase content than the WR counterpart. The amounts of β phase that were semi-quantitively calculated using RIR and image analysis are not indicative of the exact amount of this phase present in the structure; however, these values can provide a comparison.

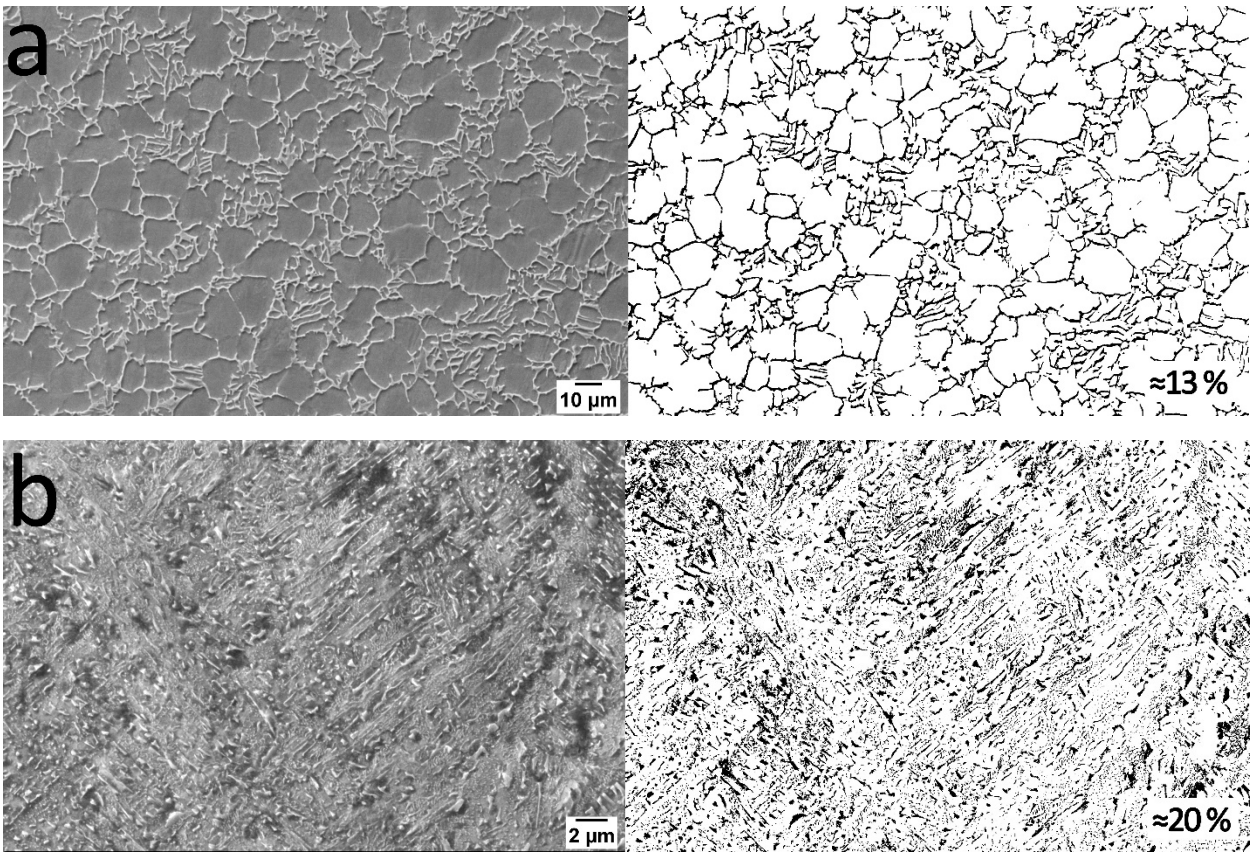

Fig. 3 Representative FE-SEM images used in ImageJ software for phase quantification analysis of WR (a) and EBM (b) Ti-G5. Images on the left are the processed images while those on the right show the binary images that represent the amount of the β phase

3.3. Electrochemical measurements

3.3.1. Open circuit potential

OCP measurements were carried out for 3600 seconds. Figure 4 (a) illustrates the OCPs of WR and EBM samples. An upward trend is seen clearly for both tested alloys followed by OCP stabilization, indicating the formation of a passive protective film on the surface of the specimens [69-71]. It is known that the more positive OCP for an alloy shows that the formed passive layer on the surface is more protective against corrosion [72]. From Fig. 4 (a), it is observed that after

350 seconds, the OCP trend of the EBM sample surpasses the WR and moves towards more positive potentials. The more positive OCP value of the EBM sample means that the spontaneously-formed passive layer on the EBM sample after 3600 seconds of OCP measurement is thermodynamically more stable and corrosion-resistant than the layer formed on the WR sample [71]. The same general OCP behavior was observed in another study for Ti-G5 in chloride-containing Ringer's solution [71].

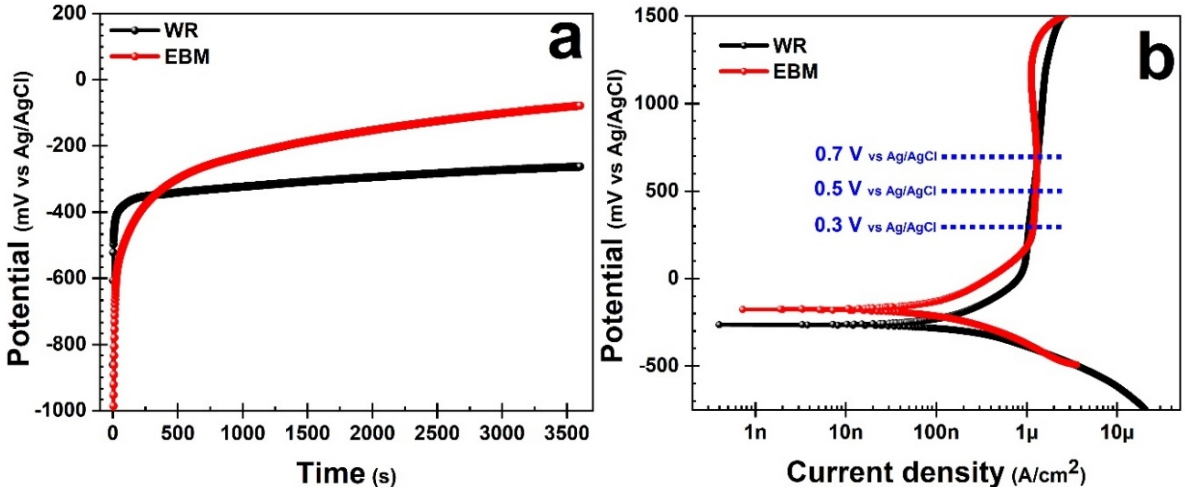

Fig. 4 (a) OCP and (b) PDP curves of WR and EBM Ti-G5 in Ringer's solution at 37±1 °C

3.3.2. Potentiodynamic polarization measurements

Figure 4 (b) shows the PDP curves of WR and EBM samples. The behavior of these two alloys is nearly the same, particularly in the passive region, with a slight difference in kinetic parameters. Both samples showed the passive behavior over a wide potential range starting from ≈100 mV up to 1500 $mV_{Ag/AgCl}$ [72]. In the passive region, there are no clear spikes, indicating that localized attack for these alloys in Ringer's solution did not happen. Using the Tafel extrapolation technique for the cathodic branch, corrosion kinetic parameters were extracted from the PDP curves. The obtained corrosion parameters, including corrosion potential (E_{corr}), corrosion current density

(i_{corr}), cathodic Tafel slope (β_c), passive current density (i_{pp}), and corrosion rate (CR) are summarized in Table 2. Because of the passive behavior of Ti, the anodic Tafel slope (β_a) was not calculated [73].

According to the corrosion parameters in Table 2, the E_{corr} value of the EBM (−0.16±0.02 $V_{Ag/AgCl}$) is nobler than the WR counterpart (−0.25±0.01 $V_{Ag/AgCl}$), which agrees with the OCP results. This indicates that the passive layer on the EBM sample has higher thermodynamic stability, with lower electrochemical surface activity and, consequently, better corrosion resistance [74-76]. Likewise, the i_{corr} value of the EBM sample (0.27±0.06 $\mu A.cm^{-2}$) is lower than for the WR sample (0.70±0.05 $\mu A.cm^{-2}$), meaning that the corrosion rate of the EBM material is less than for its WR counterpart. In terms of biomedical applications, where the lower release of metal ions is desired, lower corrosion current densities result in fewer ions released into the human body [75].

Table 2 Corrosion parameters of WR and EBM Ti-G5 in Ringer's electrolyte at 37±1 °C. Reported potentials are vs. Ag/AgCl, and data are presented with standard error

Sample	**E_{corr} (V)**	**i_{corr} (µA. cm^{-2})**	**i_{pp} (µA. cm^{-2})**	**b_c (mV/dec)**	**CR ($mm.year^{-1}$) from PDP**
WR	−0.25 ± 0.01	0.70 ± 0.05	0.98 ± 0.02	−251 ± 21.4	6.22(±0.43) $\times 10^{-3}$
EBM	−0.16 ± 0.02	0.27 ± 0.06	0.80 ± 0.02	−218 ± 10.1	2.35(±0.50) $\times 10^{-3}$

The i_{pp} values of WR (0.98 ± 0.02 μA.cm^{-2}) and EBM (0.80 ± 0.02 μA.cm^{-2}) are very close. It can also be said that the passivation of the two materials was easy since the i_{pp} values were lower than 10 μA.cm^{-2}, which is considered as a passivation current density threshold for bio-metals. At this threshold, passive films are formed in corrosive electrolytes [31].

The corrosion rate of the WR and EBM samples from PDP data was calculated using the equation in the ASTM G102-89 standard [77]:

$$CR = K \times \frac{i_{corr}}{\rho} \times EW \quad (1)$$

Where "K" is a constant (3.27×10^{-3} for CR in mm.year^{-1}), "i_{corr}" is the corrosion current density (μA.cm^{-2}), "ρ" is the density (g.cm^{-3}), and "EW" is the equivalent weight. The EW of Ti-G5 was found to be 11.90 [77]. The calculated CR values are summarised in Table 2. The CR values calculated from immersion tests (see supplementary information) and PDP are comparable for both WR and EBM Ti-G5.

Compared to the WR sample, the larger corrosion resistance of the EBM material might be attributed to its higher amount of the β phase. It is known that the oxide film formed on the β phase is of higher stability and corrosion resistance compared to the α phase [12, 30, 31, 78]. Since the β phase contains more V as a β phase stabilizer, the better corrosion resistance of this phase can be explained by its higher content of V [12, 30, 56, 79]. Therefore, the β-type titanium alloys possess better corrosion resistance compared to the α-type [12, 79]. Moreover, the α phase is more prone to selective corrosion, and its corrosion rate at the α/β interface at OCP is higher than the β phase [12, 79]. As reported in the literature, higher β phase contents result in the better corrosion resistance for the EBM samples than for the WR; also, lesser amounts of β phase contributed to the inferior corrosion resistance of some SLM samples [12, 30, 56]. As explained in [12], more β

phase in the EBM sample is the reason for increased charge transfer resistance through the double-layer, and as a result, the dissolution rate of the EBM alloy decreased [12]. According to the results of the semi-quantitative β phase analysis using ImageJ, the β phase content of the EBM sample is larger than in the WR material. Therefore, the higher content of the β phase in the EBM sample is thought to be one reason for its better corrosion resistance when compared to the WR counterpart.

3.3.3. Potentiostatic polarization measurements

In the PDP passive regions, three potentials were chosen as passive film formation potentials (E_f) for the steady growth of the passive layers. The selected potentials were 0.3, 0.5, and 0.7 $V_{Ag/AgCl}$. These potentials were chosen to investigate the passive film for a better compatibility with the body at various conditions. PS measurements were performed for 1 hour to grow a passive layer on the WR and EBM surfaces. Figure 5 (a) shows the typical current density variation with time for both WR and EBM samples at 0.3 $V_{Ag/AgCl}$. It is evident that after 3600 seconds of passivation, the current density decreased and stabilized to a value on the order of 10^{-7} μA.cm^{-2}.

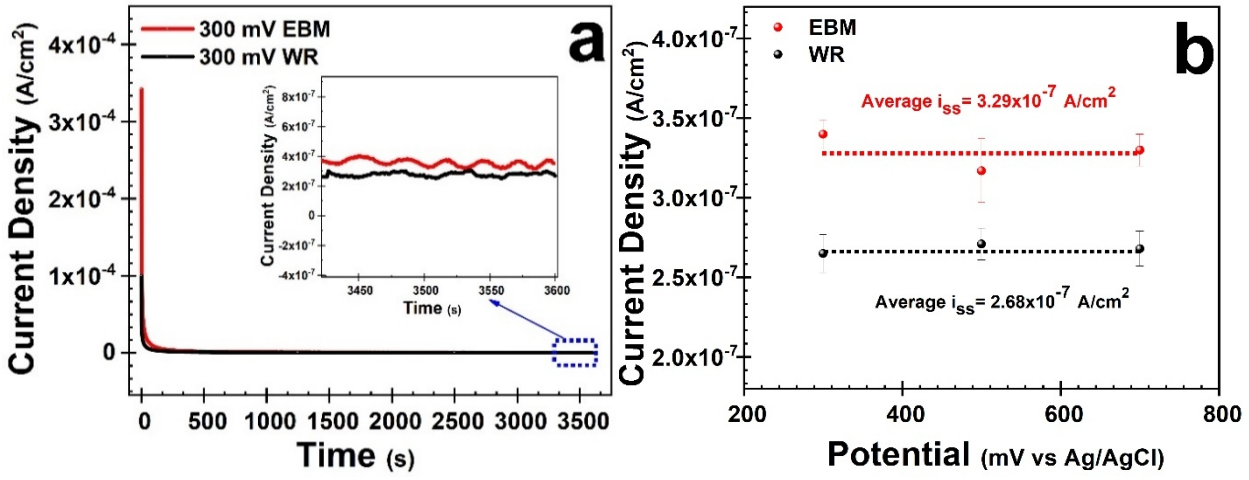

Fig. 5 (a) current-time curves of WR and EBM Ti-G5 at 0.3 $V_{Ag/AgCl}$ and (b) average i_{ss} values at 0.3, 0.5, and 0.7 $V_{Ag/AgCl}$ in Ringer's physiological solution at 37±1 °C

The initial current drop in Fig. 5 (a) can be described by the formation and growth of the passive oxide layer on the surface [31, 71, 80, 81]. The formation of the oxide layer in the primary stages of current density drop results in the resistance increase and, accordingly, current density decreases [80]. As time passes, the surface passive oxide layer improves either by increased thickness or improved compactness. This causes the inhibition of mass transport kinetics through the passive layer, which leads to the reduction of the passive current density [81]. The values of the steady-state passive current density (i_{ss}) of WR and EBM samples at three E_f of 0.3, 0.5 and 0.7 $V_{Ag/AgCl}$ are plotted in Fig. 5 (b). The average WR and EBM passive current densities were 2.68×10^{-7} and 3.29×10^{-7} $\mu A.cm^{-2}$, respectively. The current density values are on the order of 10^{-7} $A.cm^{-2}$, which is consistent with other studies for Ti-G5 in PBS and severely deformed pure titanium in Ringer's solution at 37 °C [31, 82].

The compactness of the passive film is one of the factors affecting its stability. A more compact passive film is desirable due to its better corrosion protection and ability to inhibit attachment of aggressive ions, such as chloride ions, to the passive film [71, 75]. Linear fits in the log (i) vs. log (t) plots were compared to assess the compactness of the passive layers. The variations of log (i) vs. log (t) (double-log) are shown in Fig. 6 (a), (b) and (c) for WR and EBM samples at different E_f. The following equation can be used to describe the relationship between log (i) and log (t) [71, 75]:

$$\log(i) = \log(A) - k \log(t) \quad (2)$$

Where "i" is the current density ($\mu A.cm^{-2}$),"t" represents the time, "A" refers to a constant, and "k" is the slope of the linear regions in the double-log plots, describing the compactness of the passive film. The "k" value for a compact passive film with high corrosion resistance is equal to −1, and its growth process is under electrical field control [31, 71]. However, "k=0.5" is indicative of a

passive film with porosity that was formed under diffusion controlled conditions [71, 75]. The obtained data from double-log plots shows that the "k" value for EBM is closer to −1, indicating that a more compact passive layer with higher corrosion protection was formed on the EBM material. This finding will be confirmed by EIS analysis [31].

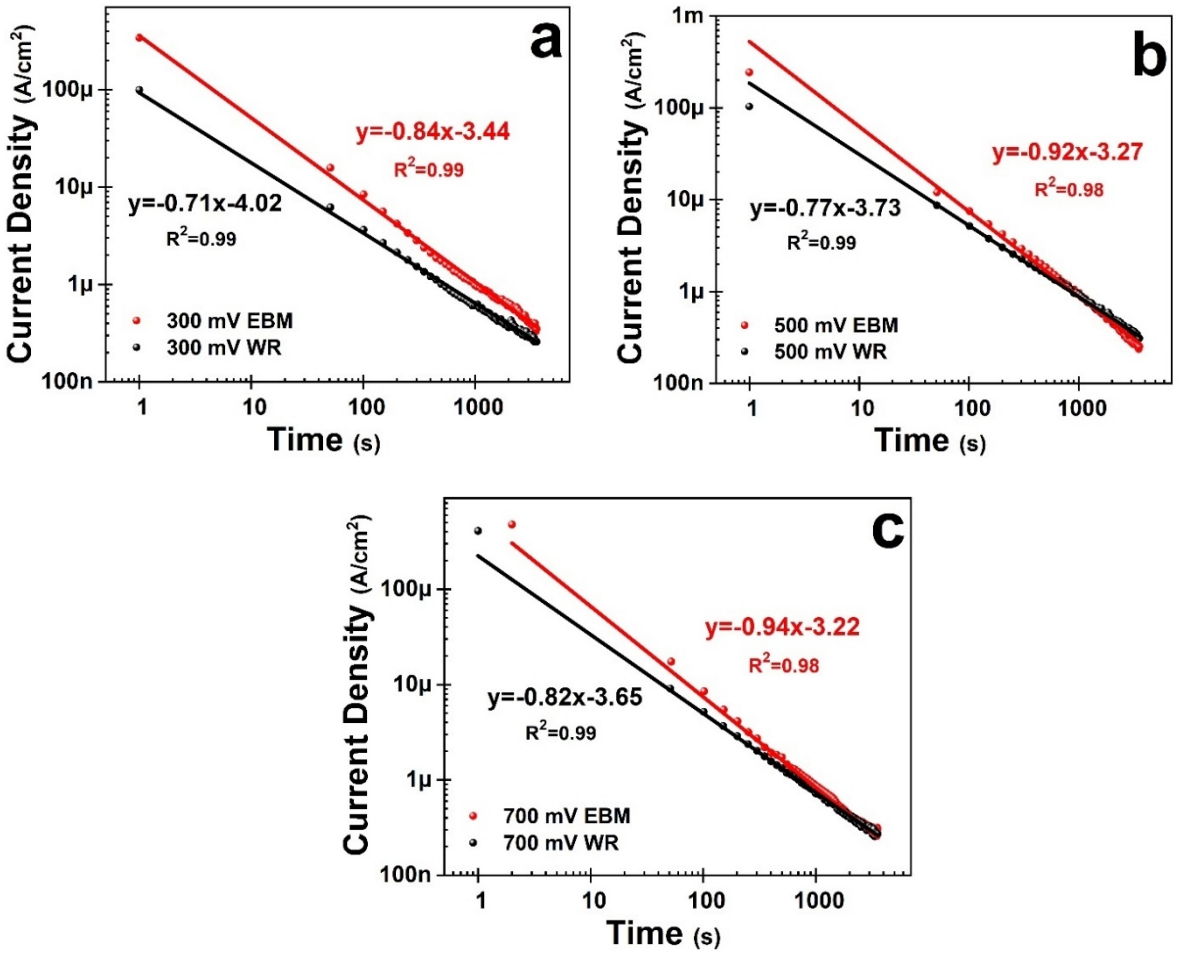

Fig. 6 Representative double-log plots of current-time curves for EBM and WR Ti-G5 in Ringer's physiological solution at 37±1 °C at passive film formation potentials of (a) 0.3 (b) 0.5 (c) 0.7 $V_{Ag/AgCl}$

3.3.4. Electrochemical impedance spectroscopy analysis

After the passive layer was formed on the surface using PS at three chosen E_f of 0.3, 0.5, and 0.7 $V_{Ag/AgCl}$, EIS was performed to investigate the properties of the passive layers. Figure 7 (a) and (b) shows the Nyquist plots of WR and EBM passive films formed at three different E_f. As can be seen from Fig. 7 (a) and (b), by increasing the E_f from 0.3 to 0.7 $V_{Ag/AgCl}$, the semicircle diameters become larger, showing the formation of a more protective passive layer for both WR and EBM alloys. At each E_f, the diameter of the EBM Nyquist curve is larger than the WR counterpart, meaning that the EBM passive layer is of higher resistance at all conditions.

Figure 7 (c) and (d) show the Bode-phase plots of WR and EBM samples at three different E_f. It is evident from the Bode modulus curves that in the high-frequency range (1-100 kHz), the impedance curve behaves independently of the frequency, inclines to be resistive, and is nearly linear with the slope of about zero. This behavior is related to the electrolyte resistance between the working and reference electrodes. Impedance values continue to rise in a nearly linear shape (slope≈ -1) in middle and low-range frequencies (1 kHz-10 mHz). Then, values on the order of 10^6 $\Omega \cdot cm^2$ are reached, showing the presence of a passive protective layer and its contribution to the impedance curve [12, 72, 80].

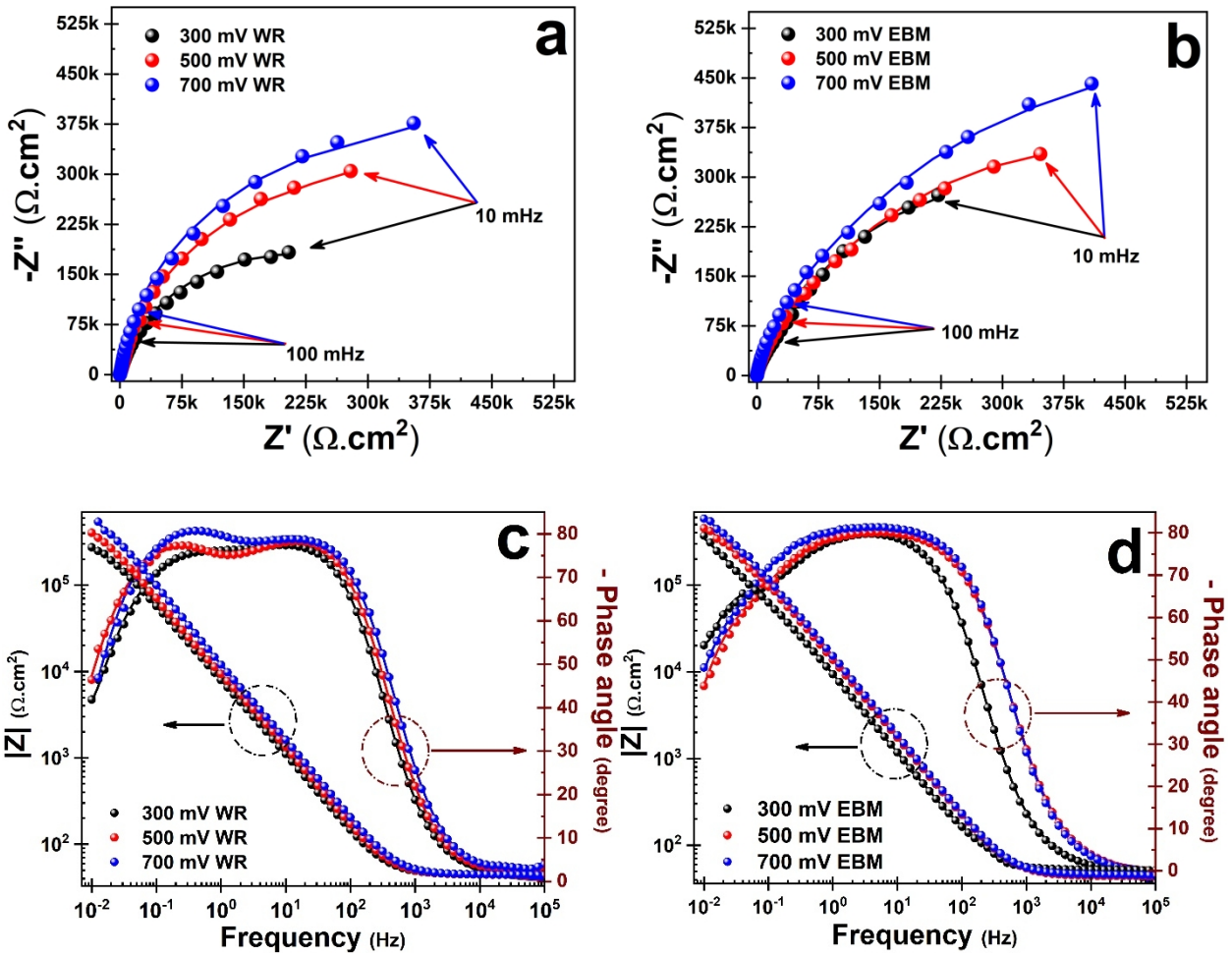

Fig. 7 (a), (b) Nyquist and (c), (d) Bode-phase modules plots of WR and EBM Ti-G5 at 0.3, 0.5, and 0.7 $V_{Ag/AgCl}$

In the high-frequency region of Bode-phase curves, the phase angle drops to values near zero. The near-zero values of the phase angles at higher frequency ranges show that the impedance is controlled by solution resistance. In the intermediate ranges of frequency, the absolute phase angle values rise. Then, in the lower frequency range, the phase angle decreases towards lower values, indicating the contribution of the passive layer resistance [12, 83]. The low-frequency region elucidates the formation of a more compact and protective inner passive layer on the surface and

the processes occurring at the electrode/electrolyte interface [80, 84–86]. Figure 7 (c) and (d) also show that the high phase angle values of about −90˚ are recorded at middle-range frequencies. The phase angle values near −90˚ and the high impedance values (on the order of $10^6\ \Omega{\cdot}cm^2$) at lower frequencies signify a near-capacitive response for both WR and EBM alloys. This is the behavior of typical passive and corrosion-resistant materials as a result of the formation of a highly stable passive film [12, 21, 87–89].

High values of impedance (on the order of $10^6\ \Omega.cm^2$) at lower frequency ranges indicate the existence of a passive barrier film, consistent with all other measurements herein and with all relevant studies on corrosion of Ti [12, 72, 80]. Overall, the larger Nyquist semicircle diameters and the higher impedance values of the EBM sample confirm its better corrosion resistance and nobler electrochemical properties than the WR counterpart.

From the Bode-phase plots, the large and broad phase angle peaks indicate an interaction of at least two time constants in the equivalent circuit [88, 90]. The presence of two time constants points to a bi-layered passive film. The Bode-phase diagrams of some results in Fig. 7 (c) and (d) show two obvious phase angle peaks, revealing at least two relaxation time constants. However, two overlapping phase angle peaks in Bode-phase diagrams of other samples indicate the formation of a duplex passive film, too. The same was also seen in other studies on Ti-G5 and Ti-Mo alloys [83, 89].

Various researchers have stated that the film on Ti is a two-layered oxide (generally TiO_2), composed of a porous outer layer and a less porous, barrier, inner layer [88, 90, 91]. As mentioned by Yang et al., the time constant in the high-frequency region represents the reactions at the film-solution interface. Whereas, the time constant in the intermediate and low range frequencies represents the passive layer properties [86]. After multiple tries to find a suitable equivalent circuit

that properly fits the experimental data, the proposed equivalent circuit with two time constants is presented in Fig. 8**Error! Reference source not found.** for WR and EBM alloys in Ringer's solution. The elements of this circuit are solution resistance (R_s), inner barrier layer resistance (R_b), outer porous layer resistance (R_p), and corresponding constant phase elements representing a shift from an ideal capacitor (CPE_b and CPE_p). The same equivalent circuit model has been reported by other researchers for Ti-Mo alloys with high porosity [83] and for WR and EBM Ti-G5 in PBS [12]. Moreover, model $R(Q_pR_p)(Q_bR_b)$ was utilized for a duplex oxide film with a sandwich structure, in which the layers are separate quasi-homogeneous oxide phases [92].

Due to the complexity of reactions and processes at the metal/solution interface, the ideal capacitor behavior is not often experimentally observed in EIS experiments for the surface oxide film. Thus, the frequency-dependent constant phase element (CPE) with the exponent "n" is usually used instead of an ideal capacitor [12, 80]. Many researchers proved that a more accurate fitting is achieved by using CPE instead of an ideal capacitor [80, 89, 93]. Results of the EIS fitting are summarized in Table 3.

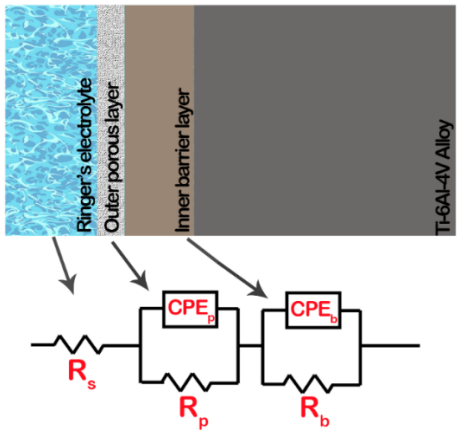

Fig. 8 Equivalent electrochemical circuit used for fitting experimental EIS data of WR and EBM Ti-G5 in Ringer's physiological solution at 37±1 °C. The passive layer on the surface is a bi-layer film

Table 3 EIS fitting parameters of WR and EBM Ti-G5 at film formation potentials of 0.3, 0.5, and 0.7 $V_{Ag/AgCl}$ in Ringer's solution at 37±1 °C. The data are presented with standard error

Sample	E_f ($V_{Ag/AgCl}$)	R_s ($\Omega.cm^2$)	R_p ($K\Omega.cm^2$)	Q_p ($\mu F.cm^{-2}$)	n_p	R_b ($M\Omega.cm^2$)	Q_b ($\mu F.cm^{-2}$)	n_b	$\chi 2$	d_b (nm)
WR	0.3	43.953 ± 0.376	1.235 ± 0.034	119.396 ± 2.775	0.937 ± 0.003	0.423 ± 0.013	34.213 ± 1.691	0.898 ± 0.006	0.009	1.552 ± 0.037
	0.5	44.223 ± 0.158	1.587 ± 0.077	52.981 ± 3.731	0.958 ± 0.002	0.698 ± 0.024	22.641 ± 2.020	0.916 ± 0.013	0.007	2.345 ± 0.177
	0.7	43.870 ± 1.167	2.692 ± 0.068	39.5498 ± 2.381	0.965 ± 0.007	0.759 ± 0.041	15.848 ± 2.473	0.983 ± 0.028	0.010	3.350 ± 0.293
EBM	0.3	45.474 ± 0.204	30.072 ± 0.966	45.836 ± 1.077	0.888 ± 0.012	0.634 ± 0.037	41.172 ± 0.425	0.909 ± 0.006	0.008	1.316 ± 0.013
	0.5	43.945 ± 0.723	46.803 ± 1.136	43.616 ± 0.392	0.900 ± 0.009	0.741 ± 0.025	26.557 ± 0.397	0.911 ± 0.004	0.010	1.999 ± 0.029
	0.7	44.958 ± 0.956	75.881 ± 1.845	41.361 ± 0.303	0.923 ± 0.010	1.021 ± 0.145	23.227 ± 0.889	0.916 ± 0.004	0.011	2.286 ± 0.081

In a study on corrosion evaluation of Ti-G5, 316 stainless steel, and CoCrMo alloys in Ringer's solution for orthopaedical applications, Songur et al. mentioned that the proposed equivalent circuit with two time constant could be an indicator of the presence of sealed pores by hydrated materials [91]. Cvijovii et al. also pointed out that the contribution of physiological solutions into the pores can increase their resistance, which is less significant for Ringer's solution due to its lower complexity. In Ringer's solution, chlorides can be absorbed into the outer porous layer but these chlorides usually form soluble compositions [94]. As it is clear from the fitting results, R_b values are much larger than R_p, showing that the corrosion resistance of the tested samples is mainly controlled by the inner barrier layer [21, 88, 90, 94]. Since the inner barrier layer properties,

with higher corrosion resistance, govern the EIS data, the effect of the porous film on impedance can be comparatively neglected [88]. While the excellent corrosion resistance of Ti alloys is associated with the inner barrier layer, the outer porous layer contributes to osseointegration. Osseointegration refers to the interaction between the bone and implant's surfaces [16]. As stated by other researchers, the existence of a porous layer for WR and EBM alloys is advantageous for biomedical applications. The presence of the porous layer is crucial to ensure the osseointegration after the implantation process in the body [21, 90, 95].

The lower R_p values for WR also show that the movement of ions inside the WR outer porous layer is more accessible, possibly due to the presence of more porosities [21, 85]. The presence of a more porous outer layer on the WR sample could possibly be due to the low amount of some incorporated oxides with the main TiO_2 component, such as Al and V oxides. In a study of variously heat treated Ti-G5 samples with different microstructures in Ringer's solution, it was shown that the incorporation of Al_2O_3 and V_2O_5 oxides homogeneously distributed in the TiO_2 matrix is a possible reason for the presence of a more resistant outer porous layer [94].

Considering that the capacitance of the inner barrier layer is the predominant capacitance in the calculation of the film thickness, the passive layer thickness (d_b) can be estimated using the following formula [96]:

$$d_b = \frac{\varepsilon\varepsilon_0 A}{C_b} \tag{3}$$

Where "d_b" is the oxide layer thickness (nm), "C_b" is the capacitance of the inner barrier layer ($\mu F.cm^{-2}$), "ε_0" is the vacuum permittivity (8.85×10^{-14} F/cm), "ε" is the dielectric constant (taken as 60 for Ti [31]), and "A" is the electrode surface area (cm^2). Calculation of thickness values (Table 3) shows that although the passive layer on the EBM sample is thinner, its corrosion

resistance is higher than its WR counterpart. The PS results also support the formation of a more compact barrier layer on the EBM material. As it is clear from the results in Table 3, the R_b values of EBM are larger than the WR at each E_f, showing that the EBM inner barrier layer is more corrosion-resistant. Overall, from the EIS results, it was shown that the passive layer on EBM provides higher corrosion protection compared to the WR.

3.3.5. Mott-Schottky analysis

Figure 9 shows the M-S plots of WR and EBM Ti-G5 at three different E_f of 0.3, 0.5, and 0.7 $V_{Ag/AgCl}$ in Ringer's physiological solution at body temperature. Similar M-S plots were previously reported for nanosheets [97] and various titanium alloys, including AMed alloys in different media such as chloride-containing solutions [35, 98], sulphate [81], and sulphuric acid solutions [99]. The slopes of the linear sections of the M-S curves represent the passive film donor density (N_d) [100]. All the lines in Fig. 9 have positive slopes, indicating the n-type semiconducting behavior of the passive films at all conditions [80].

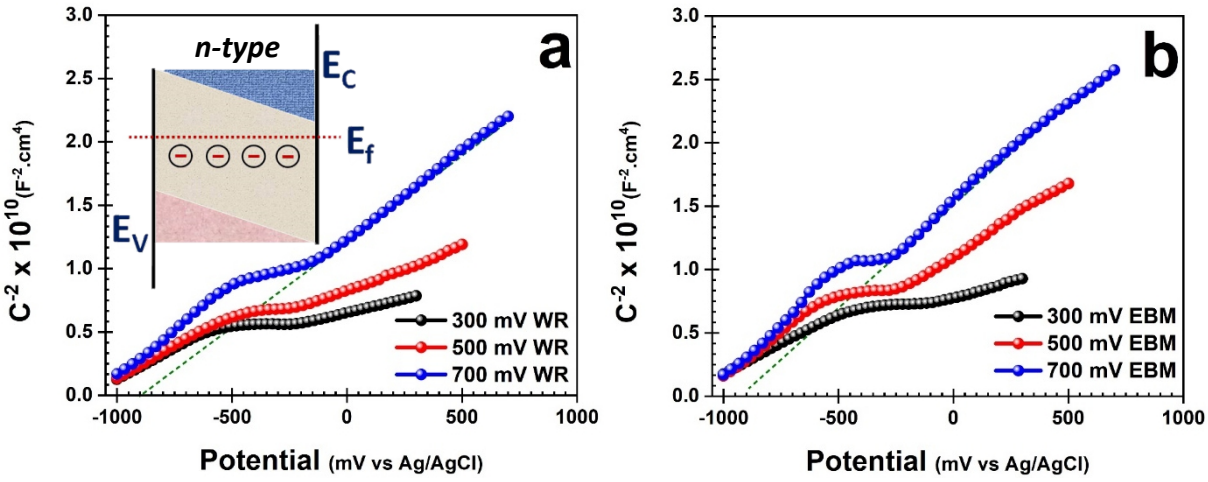

Fig. 9 Mott-Schottky plots of (a) WR and (b) EBM Ti-G5 at various passive film formation potentials in Ringer's solution at 37±1 °C. The dashed lines represent the linear fit used for donor density and flat band potential calculations

The following formula, known as the M-S relationship, shows the connection between applied potential (E) and capacitance (C) of a semiconductor [80, 101, 102]:

$$\frac{1}{C^2} = \frac{2}{\varepsilon_0 \varepsilon e N_D A^2}\left(E - E_{fb} - \frac{kT}{e}\right) \quad (4)$$

In the above equation, "e" is the electron charge (1.6×10^{-19} C) [+e for electrons and −e for holes], "A" is the surface area of the electrode (cm^2), "N_d" is the donor density in the passive film per volume (cm^{-3}), "E" is the film formation potential ($V_{Ag/AgCl}$), "E_{fb}" is the flat band potential ($V_{Ag/AgCl}$), "k" is the Boltzmann constant (1.38×10^{-23} J/K), and "T" is the absolute temperature (K). It is well known that the donor density values are inversely proportional to the slope of the linear sections in M-S plot [80]. According to Equation 4 for n-type semiconductors, N_d values can be calculated by the relationship below:

$$slope = \frac{2}{\varepsilon_0 \varepsilon_r e N_D A^2} \quad (5)$$

Flat band potentials (E_{fb}) can also be obtained from the intercept on the X-axis (extrapolation to $\frac{1}{C^2} = 0$). The linear part of the M-S curve at higher potentials corresponds to the region where the formation and growth of the passive film govern, i.e. space charge capacitance [98]. Therefore, the slopes of the linear regions at higher potential ranges were considered for the calculation of N_d and E_{fb}, and the obtained values are summarised in Table 4. The N_d values of this study are analogous with the mentioned range of 10^{18} to 10^{23} cm^{-3} in the literature [80].

The variation of capacitance with applied potential (Fig. 9) represents the electronic properties of the closest areas to the electrolyte/passive layer interface. This is because the electron depletion occurs at the regions close to the electrolyte [80] . Consequently, a region of uniform donor density is present in the areas adjacent to the metal/passive layer interface [80]. Therefore, the passive film

acts as a barrier against the electrons at the metal/passive layer interface, resulting in the corrosion inhibition and a decrease in the capacitance values.

Table 4 The donor density concentrations (N_d) and flat band potentials (E_{fb}) of WR and EBM Ti-G5 at various film formation potentials in Ringer's solution at 37±1 °C. The data are presented with standard errors

Sample	E_f ($V_{Ag/AgCl}$)	N_d ($10^{18}.cm^{-3}$)	E_{fb} ($V_{Ag/AgCl}$)
WR	0.3	5.90 ± 0.13	−1.60 ± 0.02
	0.5	3.27 ± 0.11	−1.22 ± 0.02
	0.7	2.04 ± 0.11	−0.95 ± 0.01
EBM	0.3	4.86 ± 0.26	−1.52 ± 0.01
	0.5	2.00 ±0.21	−0.95 ± 0.01
	0.7	1.43 ± 0.17	−0.93 ± 0.01

From the results of the M-S analysis, it can be realized that the slopes of the lines increased with increasing E_f for both WR and EBM alloys. As the linear slopes increase, N_d values decrease accordingly. The reason behind a decrease in N_d is the formation of a stable and more protective passive film on WR and EBM alloys [80]. It is known that the N_d values are associated with the electronic and ionic conductivity of passive films, and the relationship between the N_d and passive film conductivity is direct [35, 103].

As the N_d values decreased, the conductivity of passive films decreased as well and resulted in the formation of a more protective passive film. The lower N_d value also indicates the presence of fewer defects in the passive film. Charge carriers, which represent electron donors in an n-type semiconductor, reflect the number of defects in the space charge layer. Therefore, it can be said that the larger the charge carrier or donor density value, the higher the conductivity of passive film,

and the lower the corrosion resistance [71, 103]. Predominant defects in an n-type semiconductor refer to either oxygen vacancies or metal interstitials [71, 103].

The electrolyte in this study was Ringer's physiological solution, a chloride (Cl^-) containing media. In such a solution containing Cl^-, chloride ions may take the place of oxygen vacancies in the passive film in which the concentration of oxygen vacancies is high. This leads to the autocatalytic generation of cation vacancies [35]. The passive film dissolution rate rises as a result of the increase in the cation vacancy concentration, which can negatively influence the stability of the passive film [35]. Therefore, the ideal condition is to have fewer possible locations for the attachment of aggressive ions such as Cl^-, i.e., fewer cation vacancies. Hence, a decrease in N_d at increasing E_f shows an improvement of the WR and EBM passive film electrochemical resistances and susceptibility to localized corrosion [35]. As a comparison between WR and EBM, it can be seen from Table 4 that the N_d values of EBM are lower than WR at all conditions. Thus, it could be concluded that the corrosion resistance of the EBM sample is higher than WR, and also, the passive film on EBM is of higher stability.

The extracted values of flat-band potentials are summarized in Table 4. E_{fb} values increased to more positive potentials by increasing E_f from 0.3 towards 0.7 $V_{Ag/AgCl}$ for both WR and EBM. Nobler E_{fb} values for EBM at each E_f can also be detected. The E_{fb} value depends on the concentration of impurities and defects in the passive film [104]. According to similar studies in the literature [82, 105, 106], the lower density of defects in the EBM sample and its more positive E_{fb} seem to improve the protective behavior of the passive film with a more stable structure. The more positive E_{fb} with lower N_d was also observed for stainless steel in chromate and bicarbonate solutions, NiTi in PBS, SLM, nano-grained, and ultrasonic shot-peened Ti-G5 in Ringer's and NaCl solutions [82, 104–107].

In summary, a lower concentration of defects on the surface of the passive layer provides better corrosion protection [82]. Therefore, lower N_d values of EBM indicates the formation of a more protective passive layer on its surface. In summary of the M-S results, it was observed that the N_d values decreased with increasing E_f for both WR and EBM. The corrosion protection capability of both alloys increased with increasing E_f, i.e. a more protective passive layer with a lower density of defects formed. Moreover, at all E_f values, the lower N_d for EBM suggests its comparably better corrosion resistance than its WR counterpart.

4. Conclusions

This study evaluated the corrosion and semiconducting properties of the passive films on EBM and WR Ti-G5 in Ringer's physiological solution at body temperature.

The findings of this study are as follows:

- FE-SEM images showed that the microstructure of both EBM and WR consists of α and β phases, with larger β phase content for the EBM sample.
- OCP measurements showed that a more protective naturally-formed passive layer was developed on the EBM sample. PDP experiments also revealed that both WR and EBM materials have similar passive regions.
- The EBM's lower corrosion current density (i_{corr}=0.27 ± 0.06 μA.cm^{-2}) confirmed that the dissolution rate of the EBM material is lower than that of the WR material (i_{corr}=0.70 ± 0.05 μA.cm^{-2}).
- EIS measurements revealed that the passive film on EBM and WR materials is bi-layered and composed of an inner barrier layer and an outer porous layer. EIS fitting results

confirmed that the passive film on the EBM material is of higher resistance than that on the WR materials.

- From the results of M-S analysis, it was realized that the WR and EBM passive layers are n-type semiconductors. N_d values for WR ranged from $2.04(\pm0.11)\times10^{18}$ to $5.90(\pm0.13)\times10^{18}$ cm^{-3} for 0.3 to 0.7 $V_{Ag/AgCl}$, while this range for EBM was $1.43(\pm0.17)\times10^{18}$ to $4.86(\pm0.26)\times10^{18}$. Calculation of M-S parameters such as N_d showed that the EBM sample could form a passive layer with lower conductivity. Therefore, its corrosion resistance is higher than the WR. Overall, the EBM sample showed enhanced corrosion properties compared to the WR counterpart.

Declarations:

Funding: Not applicable

Conflicts of interest/Competing interests: The authors declare that they have no known competing financial interests or personal relationships that could have appeared to influence the work reported in this paper.

Availability of data and material: All data generated or analysed during the current study are available on reasonable request.

Code availability: Not applicable

Authors contributions:

MS contributed to conceptualization, methodology, formal analysis, investigation, data curation, and writing and preparation of the original draft; AI contributed to conceptualization, methodology, and investigation; RFS contributed to resources and writing, reviewing, and editing of the manuscript; EA contributed to conceptualization, writing, reviewing, and editing of the manuscript, supervision, and funding acquisition.

References

1. Liu Y, Schaller RF, Asselin E (2019) Effect of Fe(III) and Cu(II) on the Passivation of Ti-2 in Acidic Chloride Solutions. J Electrochem Soc 166:C76–C82. https://doi.org/10.1149/2.1021902jes

2. Tan X, Kok Y, Tan YJ, et al (2015) Graded microstructure and mechanical properties of additive manufactured Ti–6Al–4V via electron beam melting. Acta Mater 97:1–16. https://doi.org/10.1016/j.actamat.2015.06.036

3. Walker JC, Murray JW, Nie M, et al (2014) The effect of large-area pulsed electron beam melting on the corrosion and microstructure of a Ti6Al4V alloy. Appl Surf Sci 311:534–540. https://doi.org/10.1016/j.apsusc.2014.05.105

4. Safdar A, Wei L-YY, Snis A, Lai Z (2012) Evaluation of microstructural development in electron beam melted Ti-6Al-4V. Mater Charact 65:8–15. https://doi.org/10.1016/j.matchar.2011.12.008

5. Liu S, Shin YC (2019) Additive manufacturing of Ti6Al4V alloy: A review. Mater Des 164:107552. https://doi.org/10.1016/J.MATDES.2018.107552

6. Rawal S, Brantley J, Karabudak N (2013) Additive manufacturing of Ti-6Al-4V alloy components for spacecraft applications. In: 2013 6th International Conference on Recent Advances in Space Technologies (RAST). IEEE, pp 5–11

7. Sander G, Tan J, Balan P, et al (2018) Corrosion of Additively Manufactured Alloys: A Review. CORROSION 74:1318–1350. https://doi.org/10.5006/2926

8. Frazier WE (2014) Metal Additive Manufacturing: A Review. J Mater Eng Perform 23:1917–1928. https://doi.org/10.1007/s11665-014-0958-z

9. Sing SL, An J, Yeong WY, Wiria FE (2016) Laser and electron-beam powder-bed additive manufacturing of metallic implants: A review on processes, materials and designs. J Orthop Res 34:369–385. https://doi.org/10.1002/jor.23075

10. Zhang L, Liu Y, Li S, Hao Y (2018) Additive Manufacturing of Titanium Alloys by Electron Beam Melting: A Review. Adv Eng Mater 1700842:1700842. https://doi.org/10.1002/adem.201700842

11. Gong X, Anderson T, Chou K (2012) Review on Powder-Based Electron Beam Additive Manufacturing Technology. In: ASME/ISCIE 2012 International Symposium on Flexible Automation. American Society of Mechanical Engineers, pp 507–515

12. Bai Y, Gai X, Li S, et al (2017) Improved corrosion behaviour of electron beam melted Ti-6Al–4V alloy in phosphate buffered saline. Corros Sci 123:289–296. https://doi.org/10.1016/j.corsci.2017.05.003

13. Jacobs JJ, Silverton C, Hallab NJ, et al (1999) Metal release and excretion from cementless titanium alloy total knee replacements. Clin Orthop Relat Res 358:173–80

14. Jacobs JJ, Skipor AK, Black J, et al (1991) Release and excretion of metal in patients who have a total hip-replacement component made of titanium-base alloy. J Bone Joint Surg Am 73:1475–86

15. Okazaki Y, Gotoh E (2005) Comparison of metal release from various metallic biomaterials in vitro. Biomaterials 26:11–21. https://doi.org/10.1016/J.BIOMATERIALS.2004.02.005

16. Geetha M, Singh AKK, Asokamani R, Gogia AKK (2009) Ti based biomaterials, the ultimate choice for orthopaedic implants - A review. Prog Mater Sci 54:397–425. https://doi.org/10.1016/j.pmatsci.2008.06.004

17. Metikoš-Huković M, Kwokal A, Piljac J (2003) The influence of niobium and vanadium on passivity of titanium-based implants in physiological solution. Biomaterials 24:3765–3775. https://doi.org/10.1016/S0142-9612(03)00252-7

18. (1993) Corrosion fatigue resistances of surgical implant stainless steels and titanium alloy. Corros Sci 35:587–597. https://doi.org/10.1016/0010-938X(93)90193-K

19. Kim T-I, Han J-H, Lee I-S, et al (1997) New titanium alloys for biomaterials: A study of mechanical and corrosion properties and cytotoxicity. Biomed Mater Eng 7:253–263. https://doi.org/10.3233/BME-1997-7404

20. Khan MA, Williams RL, Williams DF (1996) In-vitro corrosion and wear of titanium alloys in the biological environment. Biomaterials 17:2117–2126. https://doi.org/10.1016/0142-9612(96)00029-4

21. Alves VA, Reis RQ, Santos ICB, et al (2009) In situ impedance spectroscopy study of the electrochemical

corrosion of Ti and Ti–6Al–4V in simulated body fluid at 25 °C and 37 °C. Corros Sci 51:2473–2482. https://doi.org/10.1016/J.CORSCI.2009.06.035

22. Eliaz N (2019) Corrosion of metallic biomaterials: A review. Materials (Basel) 12:. https://doi.org/10.3390/ma12030407

23. Hanawa T (1999) In vivo metallic biomaterials and surface modification. Mater Sci Eng A 267:260–266. https://doi.org/10.1016/S0921-5093(99)00101-X

24. Roh B, Macdonald DD (2019) Passivity of titanium: part II, the defect structure of the anodic oxide film. J Solid State Electrochem 23:1967–1979. https://doi.org/10.1007/s10008-019-04254-0

25. Abdeen DH, Palmer BR (2016) Corrosion evaluation of Ti-6Al-4V parts produced with electron beam melting machine. Rapid Prototyp J 22:322–329. https://doi.org/10.1108/RPJ-09-2014-0104

26. Fojt J, Fousova M, Jablonska E, et al (2018) Corrosion behaviour and cell interaction of Ti-6Al-4V alloy prepared by two techniques of 3D printing. Mater Sci Eng C 93:911–920. https://doi.org/10.1016/J.MSEC.2018.08.066

27. Mah D, Pelletier MH, Lovric V, Walsh WR (2019) Corrosion of 3D-Printed Orthopaedic Implant Materials. Ann Biomed Eng 47:162–173. https://doi.org/10.1007/s10439-018-02111-1

28. Devika D, Dass SS, Kumar Chaudhary S (2015) Characterization and Corrosion Behaviour Study on Biocompatible Ti-6Al-4V Component Fabricated by Electron Beam Melting. J Biomimetics, Biomater Biomed Eng 22:63–75. https://doi.org/10.4028/www.scientific.net/JBBBE.22.63

29. Chen LYY, Huang JCC, Lin CHH, et al (2017) Anisotropic response of Ti-6Al-4V alloy fabricated by 3D printing selective laser melting. Mater Sci Eng A 682:389–395. https://doi.org/10.1016/j.msea.2016.11.061

30. Dai N, Zhang LC, Zhang J, et al (2016) Corrosion behavior of selective laser melted Ti-6Al-4 V alloy in NaCl solution. Corros Sci 102:484–489. https://doi.org/10.1016/j.corsci.2015.10.041

31. Gai X, Bai Y, Li J, et al (2018) Electrochemical behaviour of passive film formed on the surface of Ti-6Al-4V alloys fabricated by electron beam melting. Corros Sci 145:80–89. https://doi.org/10.1016/J.CORSCI.2018.09.010

32. Zhao B, Wang H, Qiao N, et al (2017) Corrosion resistance characteristics of a Ti-6Al-4V alloy scaffold that is fabricated by electron beam melting and selective laser melting for implantation in vivo. Mater Sci Eng C 70:832–841. https://doi.org/10.1016/j.msec.2016.07.045

33. Acquesta A, Monetta T (2020) As-built EBM and DMLS Ti-6Al-4V parts: Topography–corrosion resistance relationship in a simulated body fluid. Metals (Basel) 10:1–15. https://doi.org/10.3390/met10081015

34. Wu YC, Kuo CN, Chung YC, et al (2019) Effects of electropolishing on mechanical properties and bio-corrosion of Ti6Al4V fabricated by electron beam melting additive manufacturing. Materials (Basel) 12:1466. https://doi.org/10.3390/ma12091466

35. Gai X, Bai Y, Li S, et al (2020) In-situ monitoring of the electrochemical behavior of cellular structured biomedical Ti-6Al-4V alloy fabricated by electron beam melting in simulated physiological fluid. Acta Biomater. https://doi.org/10.1016/j.actbio.2020.02.008

36. Fleck C, Eifler D (2010) Corrosion, fatigue and corrosion fatigue behaviour of metal implant materials, especially titanium alloys. Int J Fatigue 32:929–935. https://doi.org/10.1016/j.ijfatigue.2009.09.009

37. Manivasagam G, Dhinasekaran D, Rajamanickam A (2010) Biomedical Implants: Corrosion and its Prevention - A Review. Recent Patents Corros Sci 2:40–54. https://doi.org/10.2174/1877610801002010040

38. Bundy KJ (2008) Biomaterials and the chemical environment of the body. In: Joint Replacement Technology. Elsevier Ltd., pp 56–80

39. Sardana V, Burzynski J, Scuderi GR (2019) The influence of the irrigating solution on articular cartilage in

arthroscopic surgery: A systematic review. J. Orthop. 16:158–165

40. Shinjo H, Nakata K, Shino K, et al (2002) Effect of irrigation solutions for arthroscopic surgery on intraarticular tissue: Comparison in human meniscus-derived primary cell culture between lactate Ringer's solution and saline solution. J Orthop Res 20:1305–1310. https://doi.org/10.1016/S0736-0266(02)00062-1

41. Croset G, Martin G, Josserond C, et al (2021) In-situ layerwise monitoring of electron beam powder bed fusion using near-infrared imaging. Addit Manuf 38:. https://doi.org/10.1016/j.addma.2020.101767

42. Persenot T, Burr A, Martin G, et al (2019) Effect of build orientation on the fatigue properties of as-built Electron Beam Melted Ti-6Al-4V alloy. Int J Fatigue 118:65–76. https://doi.org/10.1016/j.ijfatigue.2018.08.006

43. ASTM International (2014) F3001-14 Standard Specification for Additive Manufacturing Titanium-6 Aluminum-4 Vanadium ELI (Extra Low Interstitial) with Powder Bed Fusion

44. Abramoff MD, Magalhães PJ, Ram SJ (2004) Image Processing with ImageJ. Biophotonics Int 11:36–42

45. Zakerin N, Morshed-Behbahani K (2021) In Vitro Electrochemical Behavior of Aged Ti-6Al-4V Alloy: A Trial of the Point Defect Model. Mater Today Commun 27:102327. https://doi.org/10.1016/j.mtcomm.2021.102327

46. Wu B, Pan Z, Li S, et al (2018) The anisotropic corrosion behaviour of wire arc additive manufactured Ti-6Al-4V alloy in 3.5% NaCl solution. Corros Sci 137:176–183. https://doi.org/10.1016/J.CORSCI.2018.03.047

47. Xu X, Ren X, Hou H, Luo X (2021) Effects of cryogenic and annealing treatment on microstructure and properties of friction stir welded TA15 joints. Mater Sci Eng A 804:140750. https://doi.org/10.1016/j.msea.2021.140750

48. Yazid SA, Mohd Z, Mohamad J (2018) Effect of titanium (IV) isopropoxide molarity on the crystallinity and photocatalytic activity of titanium dioxide thin film deposited via green sol – gel route. Integr Med Res 8:1434–1439. https://doi.org/10.1016/j.jmrt.2018.10.009

49. Biswas A, Dutta Majumdar J (2009) Surface characterization and mechanical property evaluation of thermally oxidized Ti-6Al-4V. Mater Charact 60:513–518. https://doi.org/10.1016/j.matchar.2008.12.014

50. Chung FH (1974) Quantitative interpretation of X-ray diffraction patterns of mixtures. I. Matrix-flushing method for quantitative multicomponent analysis. J Appl Crystallogr 7:519–525. https://doi.org/10.1107/S0021889874010375

51. Xu P, Li L, Zhang C (Sam) (2014) Microstructure characterization of laser welded Ti-6Al-4V fusion zones. Mater Charact 87:179–185. https://doi.org/10.1016/j.matchar.2013.11.005

52. Kumari R, Blawert C, Majumdar JD (2016) Microstructures and Properties of Plasma Electrolytic Oxidized Ti Alloy (Ti-6Al-4V) for Bio-implant Application. Metall Mater Trans A Phys Metall Mater Sci 47:788–800. https://doi.org/10.1007/s11661-015-3256-y

53. Ji X, Qing Q, Ji C, et al (2018) Slurry Erosion Wear Resistance and Impact-Induced Phase Transformation of Titanium Alloys. Tribol Lett 66:1–7. https://doi.org/10.1007/s11249-018-1015-0

55. Tan X, Kok Y, Toh WQ, et al (2016) Revealing martensitic transformation and α/β interface evolution in electron beam melting three-dimensional-printed Ti-6Al-4V. Sci Rep 6:26039. https://doi.org/10.1038/srep26039

56. Zhang Y, Bai S, Riede M, et al (2020) A comprehensive study on fused filament fabrication of Ti-6Al-4V structures. Addit Manuf 34:101256. https://doi.org/10.1016/j.addma.2020.101256

57. Dai N, Zhang L-C, Zhang J, et al (2016) Distinction in corrosion resistance of selective laser melted Ti-6Al-4V alloy on different planes. Corros Sci 111:703–710. https://doi.org/10.1016/J.CORSCI.2016.06.009

58. Attallah MM, Zabeen S, Cernik RJ, Preuss M (2009) Comparative determination of the α/β phase fraction in α+β-titanium alloys using X-ray diffraction and electron microscopy. Mater Charact 60:1248–1256. https://doi.org/10.1016/j.matchar.2009.05.006

59. Hayes BJ (2015) Characterization of Ti-6Al-4V Produced Via Electron Beam Additive Manufacturing. University of North Texas

60. Donachie MJ (2000) Titanium: a technical guide. ASM International

61. Barriobero-Vila P, Requena G, Buslaps T, et al (2015) Role of element partitioning on the α-β Phase transformation kinetics of a bi-modal Ti-6Al-6V-2Sn alloy during continuous heating. J Alloys Compd 626:330–339. https://doi.org/10.1016/j.jallcom.2014.11.176

62. (2017) Grain Refinement of Freeform Fabricated Ti-6Al-4V Alloy Using Beam/Arc Modulation Scott Mitzner. 536–555

63. Ge J, Yan X, Lei Y, et al (2021) A detailed analysis on the microstructure and compressive properties of selective laser melted Ti6Al4V lattice structures. Mater Des 198:109292. https://doi.org/10.1016/j.matdes.2020.109292

64. Cao S, Chu R, Zhou X, et al (2018) Role of martensite decomposition in tensile properties of selective laser melted Ti-6Al-4V. J Alloys Compd 744:357–363. https://doi.org/10.1016/j.jallcom.2018.02.111

65. Ferraro MM (2018) Quantitative Determination of Residual Stress on Additively Manufactured Ti-6Al-4V

66. Barriobero-Vila P (2015) Phase transformation kinetics during continuous heating of α+β and metastable β titanium alloys. PhD Thesis TU Vienna Austria 2015

67. Xie L, Liu C, Song Y, et al (2020) Evaluation of microstructure variation of TC11 alloy after electroshocking treatment. J Mater Res Technol 9:2455–2466. https://doi.org/10.1016/j.jmrt.2019.12.076

68. Bodunrin MO, Chown LH (2020) Towards the development of experimental (α + β) Ti-Al-V-Fe alloys. Mater Today Proc 38:663–668. https://doi.org/10.1016/j.matpr.2020.03.645

69. Sabban R, Bahl S, Chatterjee K, Suwas S (2019) Globularization using heat treatment in additively manufactured Ti-6Al-4V for high strength and toughness. Acta Mater 162:239–254. https://doi.org/10.1016/j.actamat.2018.09.064

70. Atapour M, Pilchak A, Frankel GS, et al (2010) Corrosion Behavior of Ti-6Al-4V with Different Thermomechanical Treatments and Microstructures. CORROSION 66:065004-065004–9. https://doi.org/10.5006/1.3452400

71. Xu J, Hu W, Xu S, et al (2016) Electrochemical Properties of a Novel β-Ta2O5 Nanoceramic Coating Exposed to Simulated Body Solutions. ACS Biomater Sci Eng 2:73–89. https://doi.org/10.1021/acsbiomaterials.5b00384

72. lin Liu L, Xu J, Lu X, et al (2016) Electrochemical Corrosion Behavior of Nanocrystalline β-Ta Coating for Biomedical Applications. https://doi.org/10.1021/acsbiomaterials.5b00552

73. Shi K, Zhang Y, Zhang J, Xie Z (2019) Electrochemical properties of niobium coating for biomedical application. Coatings 9:546. https://doi.org/10.3390/coatings9090546

74. McCafferty E (2005) Validation of corrosion rates measured by the Tafel extrapolation method. Corros Sci 47:3202–3215. https://doi.org/10.1016/J.CORSCI.2005.05.046

75. Pacha-Olivenza MA, Gallardo-Moreno AM, Vadillo-Rodríguez V, et al (2013) Electrochemical analysis of the UV treated bactericidal Ti6Al4V surfaces. Mater Sci Eng C 33:1789–1794. https://doi.org/10.1016/j.msec.2012.12.079

76. Liu L, Xu J, Jiang S (2016) Nanocrystalline β-Ta Coating Enhances the Longevity and Bioactivity of Medical Titanium Alloys. Metals (Basel) 6:221. https://doi.org/10.3390/met6090221

77. Kalisz M, Grobelny M, Zdrojek M, et al (2015) The hybrid graphene multilayer system (graphene/SiN/graphene) coupled with titanium alloy (Ti6Al4V) — structural, mechanical and corrosion characterisation. Thin Solid Films 596:101–110. https://doi.org/10.1016/J.TSF.2015.07.067

78. ASTM International G102-89(2015)e1 Standard Practice for Calculation of Corrosion Rates and Related Information from Electrochemical Measurements

79. Chen J-R, Tsai W-T (2011) In situ corrosion monitoring of Ti–6Al–4V alloy in H2SO4/HCl mixed solution using electrochemical AFM. Electrochim Acta 56:1746–1751. https://doi.org/10.1016/j.electacta.2010.10.024

80. Chen Y, Zhang J, Dai N, et al (2017) Electrochimica Acta Corrosion Behaviour of Selective Laser Melted Ti-TiB Biocomposite in Simulated Body Fluid. Electrochim Acta 232:89–97. https://doi.org/10.1016/j.electacta.2017.02.112

81. Munirathinam B, Narayanan R, Neelakantan L (2016) Electrochemical and semiconducting properties of thin passive film formed on titanium in chloride medium at various pH conditions. Thin Solid Films 598:260–270. https://doi.org/10.1016/J.TSF.2015.12.025

82. Zha L, Li H, Wang N (2019) Electrochemical Characterization of Anodic Oxide Film on TC11 Alloy in Sulfate Solution at High Temperature and High Pressure. 14:4546–4556. https://doi.org/10.20964/2019.05.35

83. Ansari G, Fattah-alhosseini A (2017) On the passive and semiconducting behavior of severely deformed pure titanium in Ringer's physiological solution at 37 °C: A trial of the point defect model. Mater Sci Eng C 75:64–71. https://doi.org/10.1016/j.msec.2017.02.046

84. Xie F, He X, Cao S, et al (2013) Influence of pore characteristics on microstructure, mechanical properties and corrosion resistance of selective laser sintered porous Ti-Mo alloys for biomedical applications. Electrochim Acta 105:121–129. https://doi.org/10.1016/j.electacta.2013.04.105

85. Souto RM, Laz MM, Reis RL (2003) Degradation characteristics of hydroxyapatite coatings on orthopaedic TiAlV in simulated physiological media investigated by electrochemical impedance spectroscopy. Biomaterials 24:4213–4221. https://doi.org/10.1016/S0142-9612(03)00362-4

86. (2013) Corrosion behavior of biomedical Ti–24Nb–4Zr–8Sn alloy in different simulated body solutions. Mater Sci Eng C 33:2159–2167. https://doi.org/10.1016/J.MSEC.2013.01.036

87. Yang X, Du C, Wan H, et al (2018) Influence of sulfides on the passivation behavior of titanium alloy TA2 in simulated seawater environments. Appl Surf Sci 458:198–209. https://doi.org/10.1016/J.APSUSC.2018.07.068

88. Tamilselvi S, Raman V, Rajendran N (2006) Corrosion behaviour of Ti-6Al-7Nb and Ti-6Al-4V ELI alloys in the simulated body fluid solution by electrochemical impedance spectroscopy. Electrochim Acta 52:839–846. https://doi.org/10.1016/j.electacta.2006.06.018

89. Heakal FE, Awad KA (2011) Electrochemical Corrosion and Passivation Behavior of Titanium and Its Ti-6Al-4V Alloy in Low and Highly Concentrated HBr Solutions. Int J Electrochem Sci 6:6483–6502

90. El-Taib Heakal F, Ghoneim AA, Mogoda AS, Awad K (2011) Electrochemical behaviour of Ti-6Al-4V alloy and Ti in azide and halide solutions. Corros Sci 53:2728–2737. https://doi.org/10.1016/j.corsci.2011.05.003

91. Assis SL de, Wolynec S, Costa I (2006) Corrosion characterization of titanium alloys by electrochemical techniques. Electrochim Acta 51:1815–1819. https://doi.org/10.1016/J.ELECTACTA.2005.02.121

92. Songür M, Çelikkan H, Gökmeşe F, et al (2009) Electrochemical corrosion properties of metal alloys used in orthopaedic implants. J Appl Electrochem 39:1259–1265. https://doi.org/10.1007/s10800-009-9793-6

93. Pan J, Leygraf C, Jargelius-Pettersson RFA, Lindén J (1998) Characterization of high-temperature oxide films on stainless steels by electrochemical-impedance spectroscopy. Oxid Met 50:431–455.

https://doi.org/10.1023/A:1018856808917

94. Benea L, Mardare-Danaila E, Mardare M, Celis J-P (2014) Preparation of titanium oxide and hydroxyapatite on Ti–6Al–4V alloy surface and electrochemical behaviour in bio-simulated fluid solution. Corros Sci 80:331–338. https://doi.org/10.1016/J.CORSCI.2013.11.059

95. Cvijovi I, Bajat J, Rakin M (2016) Electrochemical behaviour of Ti-6Al-4V alloy with different microstructures in a simulated bio-environment. 12–17. https://doi.org/10.1002/maco.201508796

96. Al-Mobarak NA, Al-Swayih AA, Al-Rashoud FA (2011) Corrosion Behavior of Ti-6Al-7Nb Alloy in Biological Solution for Dentistry Applications. Int J Electrochem Sci 6:2031–2042

97. Wang W, Mohammadi F, Alfantazi A (2012) Corrosion behaviour of niobium in phosphate buffered saline solutions with different concentrations of bovine serum albumin. Corros Sci 57:11–21. https://doi.org/10.1016/j.corsci.2011.12.039

98. Xu P, Milstein TJ, Mallouk TE (2016) Flat-Band Potentials of Molecularly Thin Metal Oxide Nanosheets. https://doi.org/10.1021/acsami.6b02901

99. Hazan J, Bamberger M (2020) Corrosion and Protection (Conversion Coating and Plasma Electrolytic Oxidation) of Ti6Al4V Processed by Powder Bed Fusion—Additive Manufacturing. EIS Study. Springer, Cham, pp 1317–1327

100. Liu L, Xu J, Munroe P, Xie Z (2014) Microstructure, mechanical and electrochemical properties of in situ synthesized TiC reinforced Ti5Si3 nanocomposite coatings on Ti–6Al–4V substrates. Electrochim Acta 115:86–95. https://doi.org/10.1016/j.electacta.2013.10.138

101. Liu J, Alfantazi A, Asselin E (2015) The effect of chloride ions on the passive films of titanium in sulfuric acids. Solid State Phenom 227:67–70. https://doi.org/10.4028/www.scientific.net/SSP.227.67

102. Morshed-Behbahani K, Najafisayar P, Pakshir M, Shahsavari M (2018) An electrochemical study on the effect of stabilization and sensitization heat treatments on the intergranular corrosion behaviour of AISI 321H austenitic stainless steel. Corros Sci 138:28–41. https://doi.org/10.1016/j.corsci.2018.03.043

103. Imani A, Asselin E (2021) Fluoride induced corrosion of Ti-45Nb in sulfuric acid solutions. Corros Sci 181:109232. https://doi.org/10.1016/j.corsci.2020.109232

104. Liu JC, Zhang G, Nagao S, et al (2015) Metastable pitting and its correlation with electronic properties of passive films on Sn-xZn solder alloys. Corros Sci 99:154–163. https://doi.org/10.1016/j.corsci.2015.06.036

105. Cheng YF, Luo JL (2000) Comparison of the pitting susceptibility and semiconducting properties of the passive films on carbon steel in chromate and bicarbonate solutions. Appl Surf Sci 167:113–121. https://doi.org/10.1016/S0169-4332(00)00534-1

106. Zhang CH, Song W, Wang YM, Xiao GZ (2017) Effect of Surface Strengthening on Corrosion Property of Ti-6Al-4V in 3.5% NaCl. Appl Mech Mater 853:473–477. https://doi.org/10.4028/WWW.SCIENTIFIC.NET/AMM.853.473

107. Qiu P, Gao P, Wang S, et al (2020) Study on corrosion behavior of the selective laser melted NiTi alloy with superior tensile property and shape memory effect. Corros Sci 175:108891. https://doi.org/10.1016/J.CORSCI.2020.108891

108. Chiu T, Mahmoudi M, Dai W, et al (2018) Corrosion assessment of Ti-6Al-4V fabricated using laser powder-bed fusion additive manufacturing. Electrochim Acta 279:143–151. https://doi.org/10.1016/j.electacta.2018.04.189